Measurements of flow-induced birefringence in microfluidics

Chen-li Sun[a] and Hung-Yen Huang
Department of Mechanical Engineering, National Taiwan University, Taipei 106, Taiwan

(Received 31 October 2015; accepted 4 January 2016; published online 13 January 2016)

In this study, we demonstrate the use of a microscopic circular polariscope to measure the flow-induced birefringence in a microfluidic device that represents the kinematics of fluid motion optically. Unlike the commercial birefringence microscope employed in the previous studies, our approach is able to provide direct measurement of retardance, which quantifies the difference in refractive index of the fluid experienced by the ordinary and extraordinary rays, from one single image frame. This capability facilitates unsteady full-field quantitation of flow-induced birefringence in microfluidics that has never been achieved before. At low flow rates, we find that the value of the retardance is independent of the microfluidic design and proportional to the nominal strain rates. This linearity bridges the measurement of birefringence and the deformation rate in the microflow environment, which yields the stress information of the fluid flow. In addition, the μPIV results confirm that both extensional and shear strain rates contribute to the flow-induced birefringence so that the retardance distribution can be used to represent the field of the principal strain rate in a microfluidic device. The outcome of this study proves that our approach provides a non-invasive method that enables an intuitive full-field representation of stress in the instantaneous flow field in a microfluidic device.
 [http://dx.doi.org/10.1063/1.4939949]

I. INTRODUCTION

In microscale bio-fluid mechanics, a major challenge is to measure or visualize the shear stress field that plays a critical role in blood coagulation or thrombus formation.[1,2] In the past, the stress tensor was commonly calculated via assessing the velocity field of the flow. Although the local wall shear stress can be derived from the results of the μPIV diagnosis, its applicability is limited due to its invasiveness—the addition of seeding particles required for accurate measurements of *in vivo* blood flow under high magnification imposes risk to alter the flow behaviors.[3,4]

In microfluidic environment, methods that provide fully resolved, non-invasive, direct measurements of spatio-temporal stress fields are scarce. Recent approaches include utilizing pressure-sensitive paint (PSP) to resolve the pressure data and liquid crystal technique for shear stress measurements over surfaces in microfluidic systems.[5,6] However, these coating-based methods are constrained to measurements on surface and often required tedious data reduction procedures. In comparison, flow-induced birefringence offers a straight-forward representation of the stress field, benefiting from the stress-optical law that states a linear relationship between the principal stress difference and the amount of birefringence.[7] This opto-microfluidic method has been applied to construct extensional rheometry and study molecular response of complex fluids and biofluids to flow fields.[8–11]

For flow-induced birefringence, the measuring principle relies on detecting the optical anisotropy of a fluid as a result of stress. When entering a birefringent fluid, a linearly polarized ray splits to an extraordinary ray and an ordinary ray. The ordinary ray experiences isotropic

[a]Author to whom correspondence should be addressed. Electronic mail: clsun@ntu.edu.tw

and homogeneous refractive index in the fluid, but the refractive index experienced by the extraordinary ray is direction-dependent.[12] This results in a phase difference between the ordinary ray and the extraordinary ray, which is termed retardance. Another quantity that characterizes the birefringent property of a fluid is the orientation angle, which indicates the direction of the slow optical axis. For low stresses, the stress-optical law holds which provides a way to represent spatially resolved stress field through measuring the retardance. To separate out the birefringence and the orientation, the Pathak and McKinley groups used the Metripol birefringence microscope and the ABRIO imaging system, which are both commercially available and able to produce pseudocolour map of retardance from a sequence of images.[8,10,11,13] These multi-frame approaches hinder their application under unsteady-flow condition. On the other hand, the Odell group successfully captured the birefringent response of an oscillatory extensional flow cycle from one image frame.[14–16] Nevertheless, the Riddiford and Jerrad method used in their study requires an iterative procedure to perform the retardation-birefringence transform, which is time-consuming and costly.[14]

To realize the measurements of flow-induced birefringence in a microfluidic device, we construct a circular polariscope on top of an inverted microscope by adding two polarizers and two waveplates along its light path. The configuration of the circular polariscope permits a direct interpretation of retardance from a single image.[12] In this study, we design three different minichannels that contain a cylinder or an array of cylinders to be used as the benchmark because large extensional flow in the wake of the cylinder and strong wall effects on the two sides are expected, both impose challenge on measurement method.[1,17–20] In addition, the capability of unsteady birefringence measurements of our system can be tested by the downstream instability of the cylinder. For comparison, the μPIV diagnosis is also employed to obtain the velocity field, from which the extensional and the shear rate of the flow are determined and compared to discuss their role in flow-induced birefringence.

II. WORKING PRINCIPLE

A. Stress-optical law

Birefringence in a flowing solution occurs when the microstructural network is deformed. The double refraction leads to a relative phase shift between the two orthogonal components of light, and the retardance δ can be determined from[12]

$$\delta = \int_0^h \frac{2\pi\Delta n}{\lambda} dz, \tag{1}$$

where Δn is the difference between the ordinary and the extraordinary indices of refraction, λ is the wavelength of the incident light, and h is thickness of the fluid flow layer along the direction of the light path z. For two-dimensional flow, the stress-optical law for light at normal incidence to the flow plane leads to

$$\delta = \frac{2\pi h}{\lambda}\Delta n = \frac{2\pi h}{\lambda} C\Delta\sigma = \frac{2\pi hC}{\lambda}(\sigma_1 - \sigma_2), \tag{2}$$

where C is the stress-optical coefficient, $\Delta\sigma$ is the principal stress difference, and σ_1 and σ_2 are the eigenvalues of the two-dimensional stress tensor so that

$$\Delta\sigma = \sqrt{(\sigma_{xx} - \sigma_{yy})^2 + 4\tau_{xy}{}^2}, \tag{3}$$

where σ is the normal stress and τ is the shearing stress. In the double subscript notation, the first subscript indicates the normal direction of the plane on which the stress acts, and the

second subscript indicates the direction of the stress. Once the retardance is measured, we are able to obtain the stress information in the fluid flow through Eq. (2).

B. Experimental setup

Our schematic to measure the flow-induced birefringence in a microfluidic device is given in Fig. 1. A circular polariscope is configured on top of an inverted microscope (DM IL LED, Leica Microsystems) by adding four optical elements: two linear polarizers (10LP-VIS-B, Newport) and two quarter waveplates (10RP34, Newport) as arranged in Fig. 1. The linear polarizer nearest the light source is called the polarizer, while the second linear polarizer is referred to as the analyzer. The incident light first passes through the polarizer and the quarter waveplate A to generate a circularly polarized ray. After being transmitted through the microfluidic device, the circularly polarized ray propagates through the quarter waveplate B then the analyzer.

If the angle between the optical axes of the first polarizer and the analyzer is 90°, the light vector of the linearly polarized ray $\mathbf{E}_r$ can be expressed by

$$\mathbf{E}_r = \mathbf{R}(\xi)\mathbf{J}\mathbf{R}(-\xi)\mathbf{E}, \tag{4}$$

where $\mathbf{E}$ is the light vector of the incident ray, $\mathbf{R}(\xi)$ is the rotation matrix for an orientation angle ξ, and $\mathbf{J}$ is the Jones matrix for the first polarizer. Because the optical axis of the quarter waveplate A is oriented at 45° with respect to that of the analyzer, the waves upon entering the microfluidic device $\mathbf{E}_{QA}$ can be expressed as[12]

$$\mathbf{E}_{QA} = \frac{E}{\sqrt{2}}\begin{bmatrix} \cos\omega t \\ \cos(\omega t + \pi/2) \end{bmatrix}, \tag{5}$$

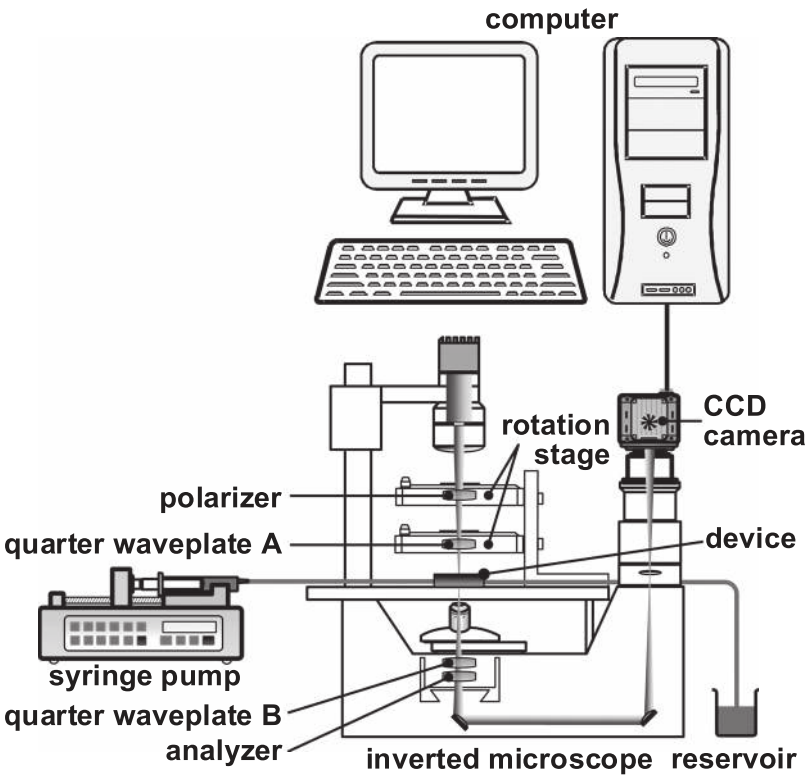

FIG. 1. Experimental setup.

where ω is the circular frequency of the wave. Assuming that the flow-induced birefringence in the microfluidic device exhibits the optical properties of a waveplate with a relative phase shift of δ and an orientation angle of θ, the light emerging from the microfluidic device $\mathbf{E}_s$ is described by

$$\mathbf{E_S} = \frac{E}{2}\begin{bmatrix} \cos(\theta+\omega t)+\sin(\theta+\omega t) \\ \cos(\theta+\omega t+\delta)-\sin(\theta+\omega t+\delta) \end{bmatrix}. \tag{6}$$

After the light propagates through the quarter waveplate B with its optical axis oriented at -45° with respect to that of the analyzer, the emerging light vector $\mathbf{E}_{QB}$ becomes

$$\mathbf{E_{QB}} = \frac{E}{2\sqrt{2}}\begin{bmatrix} \cos(2\theta+\omega t)-\cos(\delta+2\theta+\omega t)+\sin\omega t+\sin(\delta+\omega t) \\ -\cos(2\theta+\omega t)+\cos(\delta+2\theta+\omega t)+\sin\omega t+\sin(\delta+\omega t) \end{bmatrix}. \tag{7}$$

Finally, the light passes through the analyzer. The light vector transmitted by the analyzer $\mathbf{E}_A$ is given by

$$\mathbf{E}_A = \frac{E}{4}\begin{bmatrix} \sin(\omega t)+\cos(\omega t)+\sin(\delta+\omega t)+\cos(\delta+\omega t)-\sin(\delta+2\theta+\omega t)-\cos(\delta+2\theta+\omega t) \\ 0 \end{bmatrix}. \tag{8}$$

Because the intensity of light is proportional to the square of the amplitude of the light wave, the intensity ratio of the light source I_0 to the light emerging from the analyzer I_c can be related to the retardance by

$$\frac{I_c}{I_0} = \frac{\int_0^{2\pi}|\mathbf{E}_A|^2 d(\omega t)}{\int_0^{2\pi}|\mathbf{E}|^2 d(\omega t)} = \sin^2\left(\frac{\delta}{2}\right). \tag{9}$$

For the configuration of the circular polariscope, the intensity is independent of the orientation angle θ. Therefore, Eq. (9) provides a simple way to quantify the retardance δ of the flow-induced birefringence by recording one single image and a reference image. This single-image approach not only facilitates to estimate the retardance distribution intuitively before further post processing but also enables transient measurements. Without adjusting the position of any optical element, a sequence of images can be recorded to investigate the development of retardance with time in a microfluidic device.

The success of the proposed approach relies on the validity of Eq. (1). Since there is an upper bound of stress beyond which the linear stress-optical rule no longer holds, the measuring range of stress is confined. In addition, the time required to re-establish thermodynamics equilibrium in fluid puts a limit on the temporal resolution of our system.[21,22] On the other hand, the minimal discernable stress difference is influenced by the pixel depth in the acquired image, the channel depth, and the stress-optical coefficient. To improve the stress resolution, higher pixel depth, larger stress-optical coefficient, or deeper channel is preferred. The results obtained by our approach represent the accumulation of birefringence through the fluid layer or the average over the channel depth. Although the proposed technique cannot be applied to diagnose three-dimensional flow in its current configuration, the depth-resolved birefringence can be realized by tomography.[7,23]

In this study, we use a 2.5× objective (N PLAN, Leica, NA = 0.07) and a CCD camera (MotionPro X-3, Integrated Design Tool) connected to the microscope via a 1× adaptor to acquire the images. The 10-bit images are processed by a program implementing the Matlab Image Processing Toolbox (Mathworks). The grayscale readouts are divided by the exposure time in order to determine the light intensities. A syringe pump (kds210, KD Scientific) is employed to deliver the working fluid to the microfluidic device. Prior to each experiment, the reference image is acquired when fluid remains quiescent in the minichannel and both the

quarter waveplate B and the analyzer are removed from the optical path. The light source is re-calibrated to ensure the average intensity of the reference image is consistent under different condition. The quarter waveplate B and the analyzer are then re-installed in order to commence the experiment.

C. Device and working fluids

From a molding method, the microfluidic devices used in this work are made of PDMS (polydimethylsiloxane) material which exhibits birefringence when it is deformed.[24] To eliminate this unwanted effect, the stiffness of the channel material is increased by adjusting the ratio of the liquid PDMS and the cross-linking agent.[25] The channel is then checked by pumping in water, a non-birefringent fluid, and ascertained that no birefringence is observed. The PMMA (polymethylmethacrylate) mold is micromachined by a CNC (computer numerical control) milling machine. Three different microfluidic designs are tested, as shown in Fig. 2. Channel #1 and channel #2 both contain a single cylinder in the middle of the minichannel. The widths are 4 mm and 2 mm, respectively. Channel #3 comprises a linear array of seven cylinders with a pitch of 2 mm, and the fourth cylinder is positioned to the centre of the 2 mm wide channel. For all three channels, the diameter of the cylinders is 1 mm, the minichannel

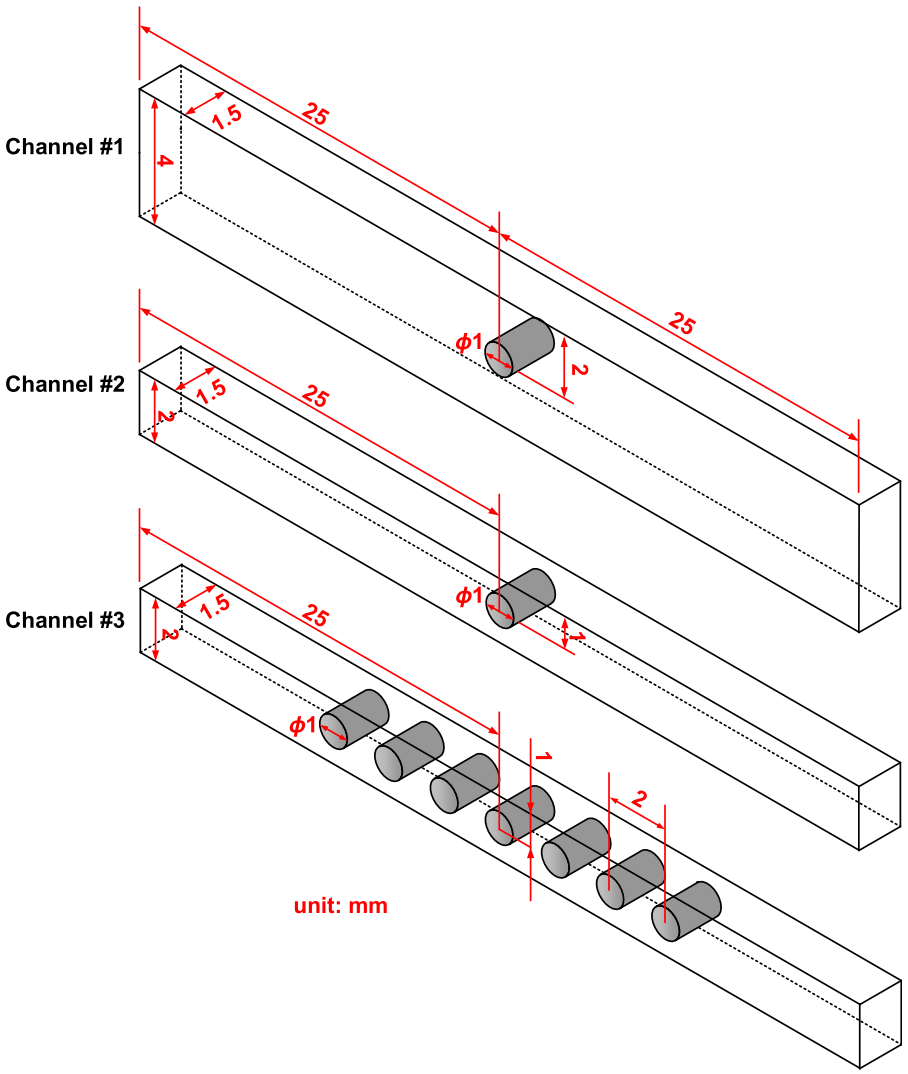

FIG. 2. Detailed dimensions of the microfluidic devices.

length is 50 mm, and the depth is 1.5 mm. The inlet and outlet of the minichannel are connected to the syringe pump via Teflon tubes with an inner diameter of 0.8 mm. Ideally, the proposed method can be applied to smaller channel size. As long as the flow-induced birefringence is sufficiently large and the Nyquist sampling criterion is satisfied for a given objective, the spatial resolution of our system is diffraction limited.[26] However, the magnification is indirectly constrained by the sensitivity of the system if the flow field fluctuates rapidly with dim birefringence. When the signal to noise ratio (S/N) becomes the limiting factor, lower magnification objective is more desirable among lenses with the same NA because signal intensity decreases with the square of the magnification factor.[26] Even though extended exposure or binning may help to recover weak signal, the improvement in S/N comes at the expense of imaging blurring and reduced spatial resolution.[26]

As an approximation, the average shearing deformation of the fluid is represented by the nominal strain rate at the gap between the cylinder and the wall of the minichannel, which is defined as

$$\varepsilon_0 = \frac{Q}{(W-D)Dh}, \tag{10}$$

where W and h are the width and depth of the channel, D is the diameter of the cylinder, and Q is the volumetric flow rate. During the experiments, the flow rate varies from 0.02 to 5.4 ml min^{-1}. Using the zero-shear viscosity to define the Reynolds number, the range of the corresponding Reynolds number is between 6.9×10^{-7} and 2.3×10^{-3}.

For the measurements of flow-induced birefringence, the working fluids have to be transparent and capable of inducing substantial birefringence with good linearity. In this study, three different working fluids are tested. The first solution is a blend of 30 mM CTAB (cetrimonium bromide) and 240 mM NaSal (sodium salicylate). The second solution is composed of 100 mM CPyCl (cetylpyridinium chloride) and 60 mM NaSal. The third solution consists of 100 mM CPyCl, 50 mM NaSal, and 100 mM NaCl (sodium chloride). The rheological and rheo-optical properties of the test fluids are well documented in literatures.[1,8,11,17] For all three tested fluids, the Maxwellian relaxation time is on the order of 10^{-1} s to 1 s. The densities are comparable to that of water, and the stress-optical coefficients have a reasonable order of magnitude and remain constant in a wide range of shear rate. For fluids which appear non-birefringent such as water, it is possible to add colloidal nanorod suspension to produce measurable birefringence.[27,28]

D. μPIV diagnosis

To compare the flow-induced birefringence results to the kinematics of the fluid motion, μPIV diagnosis is also carried out. Microparticles with a mean diameter of 5 μm and a density of 1030 kg m^{-3} (polyamide seeding particles, Dantec Dynamics) are seeded to the working fluid. The particle concentration is 2.97×10^7 particles ml^{-1} so that there are approximately 6 particles in each interrogation area after three-pass grid refining of the 16×16 pixels ($4 \times 46\,\mu\text{m}^2$) cell.[29] The exposure time is set to 30 μs, and the frame rate varies from 600 to 2000 fps, depending on the flow rate of the working fluid. To ensure that the seeding particles follow the flow, the time scale for inertial acceleration of the particle has to be much smaller than the Maxwellian relaxation time.[30] Estimated from the velocity lag of a particle in a continuously accelerating fluid, the characteristic time of the particle inertia is about 1.43 μs, much lower than the Maxwellian relaxation times of the working fluids used in this study.[29] PIVLab is utilized to resolve the velocity field,[31] from which the magnitudes of extensional rate ε_e, shear strain rate ε_s, and the principal strain rate ε_p are calculated as

$$\varepsilon_e = \sqrt{\left(\frac{\partial u}{\partial x}\right)^2 + \left(\frac{\partial v}{\partial y}\right)^2}, \tag{11a}$$

$$\varepsilon_s = \sqrt{\left(\frac{\partial u}{\partial y} + \frac{\partial v}{\partial x}\right)^2}, \tag{11b}$$

$$\varepsilon_p = \sqrt{\left(\frac{\partial u}{\partial x} - \frac{\partial v}{\partial y}\right)^2 + \left(\frac{\partial u}{\partial y} + \frac{\partial v}{\partial x}\right)^2}. \tag{11c}$$

To produce the pathlines, superposition is performed on 100 successive images. After incorporating error propagation, the overall uncertainties of the measured quantities are summarized in Table I.[32] The uncertainty of the velocity field is evaluated by comparing the μPIV results in a straight channel to the analytical solution using the Ellis model.[8] For the retardance measurement, the accuracy of Eq. (9) relies on correctly positioning each optical element so that its overall uncertainty is influenced by the precision of the rotation stage. The overall uncertainties of velocity, nominal, extensional, shear, and principal strain rate also depends on the dimension precision of the microfluidic device due to error propagation.

III. RESULTS AND DISCUSSION

A. Retardance vs. nominal strain rate

The variation of retardance distribution with the increase in the nominal strain rate is depicted in Fig. 3 for the CTAB:NaSal solution near the first two cylinders in channel #3. At $\varepsilon_0 = 1.11\,s^{-1}$, a thin symmetric region of $\delta \sim 0.2$ rad surrounds the first cylinder, covering from the front ($\theta_c = 0°$) to $\theta_c = \pm 120°$. Two faint striations are stretched and aligned side by side between the neighbouring cylinders. As they extend downstream, these two striations eventually divert and connect to the two sides ($\theta_c = \pm 30°$) of the second cylinder. As a result, a triangular region of low retardance is found near the nose of the second cylinder. When the nominal strain rate increases, the magnitude of the retardance increases correspondingly and its band widens. In the wake region, the two striations become more separate from each other and a third strand with moderate retardance emerges along the centerline. This central strand is ascribed to the extensional and compressive deformation as fluid stretches from the rear stagnation toward the nose of the following cylinder. The maximal retardance is found at $\theta_c = 90°$ of the first cylinder. When the nominal strain rate reaches $4.44\,s^{-1}$, the upstream starts to fluctuate temporally and the distribution of the flow-induced birefringence loses its symmetry. In addition, the retardance no longer augments with the nominal strain rate monotonically. At $\theta_c = 90°$ of the first cylinder, the retardance is 0.5 rad for $\varepsilon_0 = 3.33\,s^{-1}$ but decreases to 0.4 rad as ε_0 increases to $6.67\,s^{-1}$.

For all working fluids, the flow-induced birefringence in different devices is measured and the retardance at the top of the first cylinder ($\theta_c = 90°$), where fluid velocity reaches a maximum, is plotted in Fig. 4. We find that the magnitude of the retardance at this location is nearly independent of the design of the microfluidic device. Moreover, the retardance is proportional to the nominal strain rate below a certain ε_0. For the CTAB:NaSal solution, a linear relationship

TABLE I. Overall uncertainties of measurements and calculated quantities.

Quantity	Overall uncertainty (%)
Intensity, I	±1.6
Retardance, δ	±7.2
Volumetric flow rate, Q	±0.05
Nominal strain rate, ε_0	±4.4
Velocity, u	±6.4
Extensional rate, ε_e	±6.5
Shear rate, ε_s	±12.9
Principal rate, ε_p	±14.4

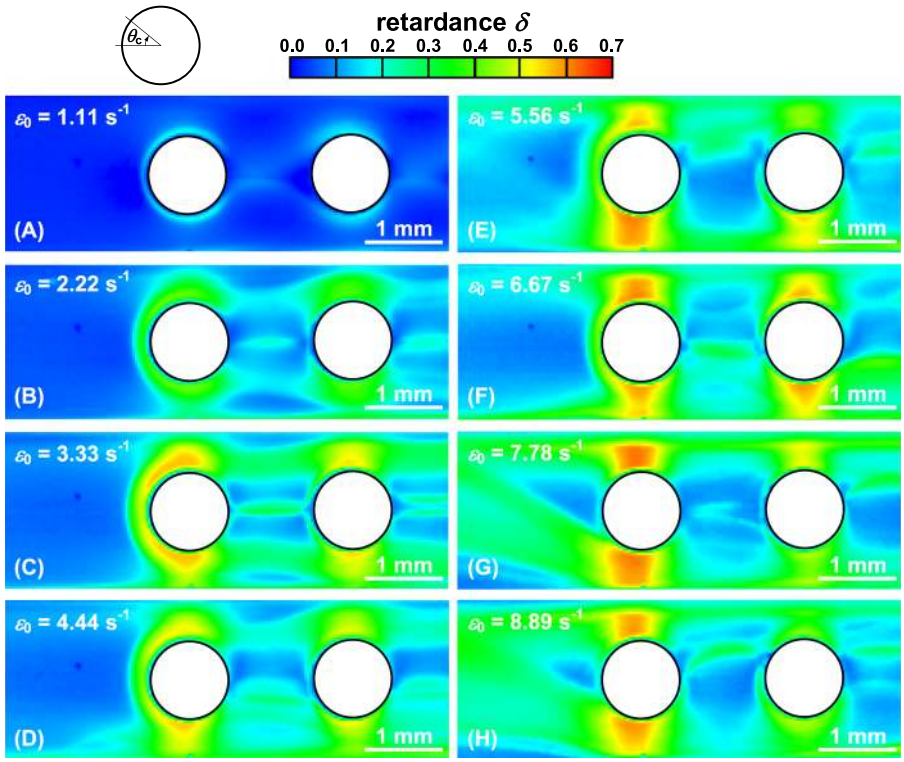

FIG. 3. Variation of the retardance distribution in channel #3 with the nominal strain rate for the CTAB:NaSal solution. The flow is from left to right.

between δ and ε_0 is found for $\varepsilon_0 \leq 3.42\,\mathrm{s}^{-1}$. As the nominal strain rate exceeds $4\,\mathrm{s}^{-1}$, the retardance exhibits some fluctuation and its magnitude drops with the nominal strain rate. This may be ascribed to the elastic instability[1,17]—sudden fluid rupture found in the wake of the cylinder leads to the temporal variation and a plunge of flow-induced birefringence. In contrast, the reduction of the retardance at large nominal strain rate is not prominent for the CPyCl:NaSal and CPyCl:NaSal:NaCl solutions. Rather, there exists a retardance plateau, where δ remains nearly unchanged with the nominal strain rate. At large ε_0, only mild unsteadiness is found for the CPyCl:NaSal solution and flow remains quite stable for the CPyCl:NaSal:NaCl solution. Because the shear banding behaviour of the working fluids, a larger shear rate is found near the wall. As a result, molecular alignment with the flow is saturated and the retardance plateau occurs. The CPyCl:NaSal solution enters the retardance plateau at $\varepsilon_0 > 5.6\,\mathrm{s}^{-1}$, much higher than the onset deformation rate of shear banding.[8] On the other hand, adding brine to the blend of the CPyCl:NaSal system actually makes the micelle more flexible and the retardance plateau appears in $\varepsilon_0 > 20\,\mathrm{s}^{-1}$. Comparing with the other two solutions, the linear region expands over

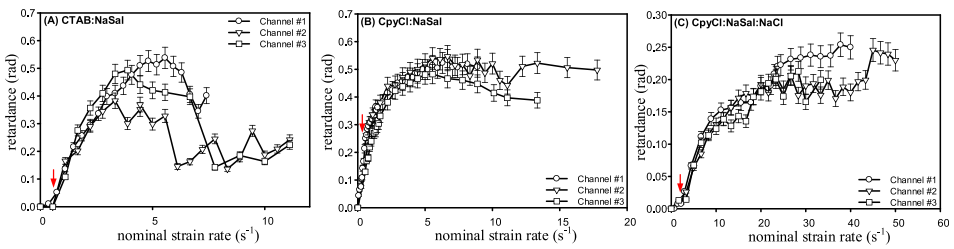

FIG. 4. The variations of retardance at the top of the first cylinder with the nominal strain rate for (a) CTAB:NaSal, (b) CPyCl:NaSal, and (c) CPyCl:NaSal:NaCl in different microfluidic devices. The red arrows indicate the onset breakdown of the stress-optical rule predicted by the reciprocal of the Maxwellian relaxation time of the fluid.

a wider range of strain rate and the maximal retardance is much lower when the CPyCl:NaSal:NaCl solution is employed.

For the CTAB:NaSal, CPyCl:NaSal, and CPyCl:NaSal:NaCl solutions, the upper limits of the nominal strain rates that confine the linear region are 3.34, 1.24, and $12\,s^{-1}$, respectively. All of these critical values are much larger than those found in Ober *et al.*[8] using the ARES rheometry with a Couette cell. Although the nonlocal effects arisen from the confined geometry of the microfluidic devices may play a role in stress propagation across the interface,[33] the linearity between δ and ε_0 still holds at shear rates higher than the onset of nonlinear rheological behavior. Therefore, the breakdown of the linearity falls on the stress plateau for the two CPyCl:NaSal systems and behind the onset of shear thinning for the CTAB:NaSal solution. Nevertheless, even in the nonlinear region, the flow-induced birefringence is able to provide some information of the stress field in a stable zone near the low shear band, where the stress still increases with the strain rate.

For all the working fluids, the linear region in Fig. 4 provides the bounds to a valid range in which the deformation of fluid filaments in a microfluidic device can be mapped from measuring the retardance with our approach. If we regard the shear rate as the input of our instrument for the flow-induced birefringence measurements, the linear region in Fig. 4 leads to a sensitivity of 0.133, 0.283, and 0.012 rad s for the CTAB:NaSal, CPyCl:NaSal, and CPyCl:NaSal:NaCl solutions, respectively. Hence, using the CPyCl:NaSal solution to measure retardance is able to obtain the highest sensitivity, while probing the flow field with the CPyCl:NaSal:NaCl solution offers a wider measuring range of strain rate. If other fluid is used, the sensitivity, the measuring range, and the minimal discernable strain rate or stress difference are changed accordingly.

B. Comparison of birefringence and μPIV results

To further examine the validity of our birefringence measurement, the μPIV diagnosis is applied to obtain the full-field velocity representation in the microfluidic devices, from which the extensional, shear, and principal strain rate are determined and compared. Figs. 5 and 6 depict the comparison between the flow-induced birefringence and the μPIV results for the CPyCl:NaSal solution in channel #1 at $\varepsilon_0 = 1.48\,s^{-1}$ and the CPyCl:NaSal:NaCl solution in channel #3 at $\varepsilon_0 = 10\,s^{-1}$, respectively. In both figures, the nominal strain rate stays within the linear region for the corresponding fluids. From Figs. 5 and 6, high similarity is found between the retardance and the principal strain, i.e., regions with large retardance usually associate with high principal strain rate. In Figs. 5(a) and 5(c), the band of flow-induced birefringence in the raw image is much narrower than that of the retardance. This is because the retardance is not linearly proportional to the image intensity obtained by the circular polariscope configuration. Because of the square of the sine in Eq. (9), a small change in I_c/I_0 leads to a large variation of δ when I_c/I_0 is below 0.15 or above 0.85. As a result, the cylinder is surrounded by a thick band of high retardance and followed by an extended tail with sharp edge. When fluid flows toward the nose of the cylinder, the fluid is decelerated and a stagnation point is formed at $\theta_c = 0°$. As passing through the cylinder, the stationary fluid at $\theta_c = 0°$ is first accelerated to its maximum velocity at $\theta_c = \pm 90°$ and then is decelerated back to zero velocity at the rear of the cylinder ($\theta_c = 180°$). Therefore, large extensional strain rate is found in $-73° < \theta_c < 73°$ in front of the cylinder and spreads from $\theta_c = \pm 100°$ to $\pm 170°$ behind the cylinder. On the other hand, shear strain rate starts to grow from $\theta_c = \pm 7°$ and reaches its maximum near $\theta_c = \pm 90°$. The shear strain rate decreases as the fluid moves to the back of the cylinder and moderate shear rate is found to extend along the centreline of the minichannel. In the wake region, this sheared flow is evidently exhibited in the birefringent results. There exists a very low retardance region right behind the cylinder because birefringence is resulted from the strain accumulated by the fluid as it flows past the cylinder.[1] When fluid is stretched in the wake, the extensional deformation is built up and the birefringent strand emerges a distance downstream of the cylinder. The combined contribution of the extensional and shear strain rate leads to the resemblance between the distributions of the retardance and the principal strain rate. In Figs. 5(a) and 5(c), the triangular stagnation zone behind the cylinder is successfully represented by the low

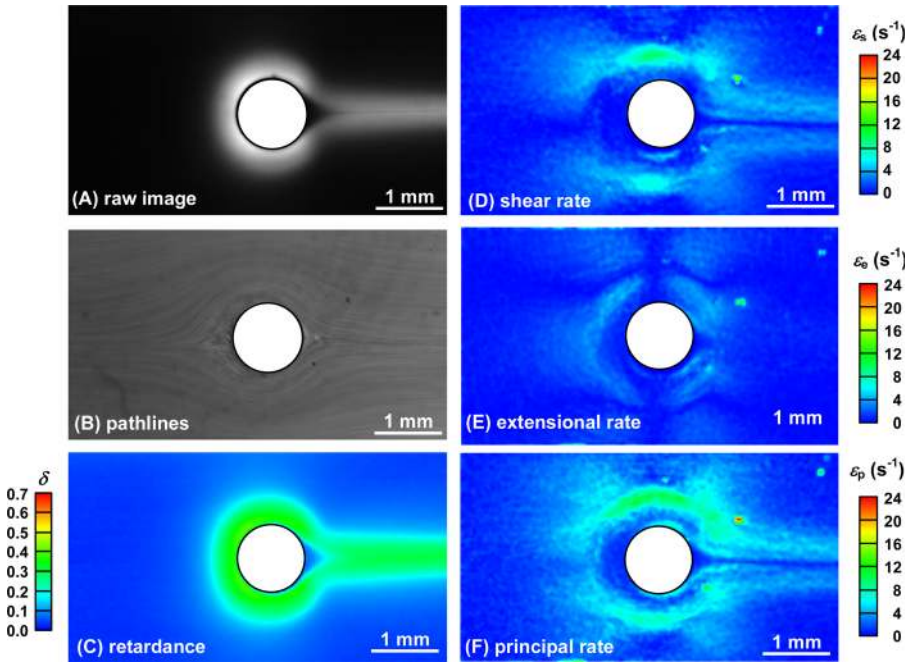

FIG. 5. Comparison of the flow-induced birefringence and PIV results for the CpyCl:NaSal solution in channel #1, $\varepsilon_0 = 1.48\,s^{-1}$: (a) the original flow-induced birefringence image taken by our system, (b) the pathlines of μPIV particles obtained by image superposition, (c) the pseudocolour map of retardance, (d) the shear strain rate, (e) the extensional strain rate, and (f) the principal strain rate. The flow is from left to right.

birefringence region. This triangular region of low retardance is more evident in Fig. 5 than that in Fig. 3 because the nominal strain rate is smaller in Fig. 5. Therefore, the CpyCl:NaSal solution experiences less deformation so that a longer distance is required to accumulate sufficient strain. In contrast, pathlines in Fig. 5(b) do not depict apparent flow separation. The μPIV diagnosis fails to resolve regions of high deformation, such as the large compression near the front of the cylinder either, and creates a C-shaped region of low principal strain rate surrounding the cylinder.

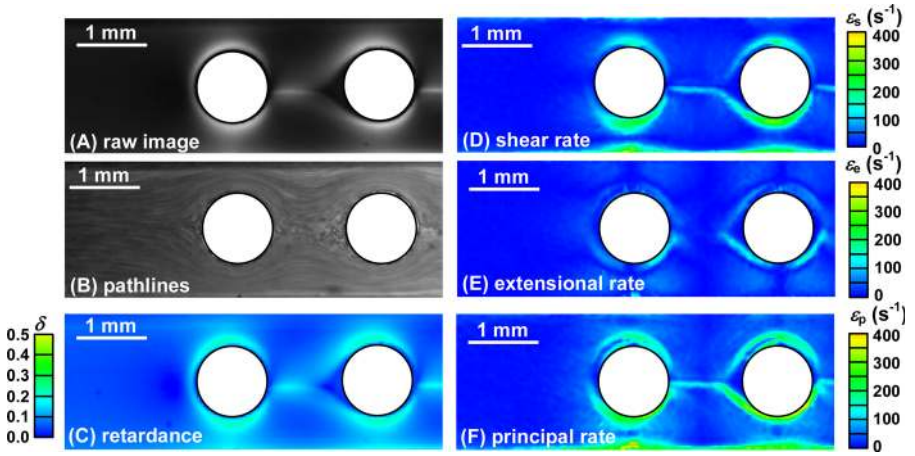

FIG. 6. Comparison of the flow-induced birefringence and PIV results for the CPyCl:NaSal:NaCl solution in channel #3, $\varepsilon_0 = 10\,s^{-1}$: (a) the original flow-induced birefringence image taken by our system, (b) the pathlines of μPIV particles obtained by image superposition, (c) the pseudocolour map of retardance, (d) the shear strain rate, (e) the extensional strain rate, and (f) the principal strain rate. The flow is from left to right.

Albeit the utilization of the image deformation scheme, the μPIV measurements suffer from large errors and high vector rejection rate in the presence of large velocity gradient.[29,34] Since shear banding takes place in $\varepsilon_0 > 0.3\,s^{-1}$ for the CPyCl:NaSal solution, the corresponding stress field may be overshot if we apply the stress-optical law on the retardance. Yet, the flow-induced birefringence shown in Fig. 5(a) and 5(c) faithfully depicts the fluid deformation near the cylinder wall, which cannot be unveiled by the μPIV diagnosis.

For the CPyCl:NaSal:NaCl solution flowing in channel #3 at $\varepsilon_0 = 10\,s^{-1}$, the flow-induced birefringence and μPIV results are shown in Fig. 6. Comparing with the other two working fluids, the CpyCl:NaSal:NaCl solution is less birefringent and its fluid flow more stable. Therefore, the retardance band enclosed the cylinder is relatively narrow even though the corresponding strain rates are quite large. Contrary to the case of the CPyCl:NaSal solution, the width of the birefringence strand surrounding the cylinder is not uniform for the CPyCl:NaSal:NaCl solution. Rather, the strand is thin near the nose and the back of the cylinder ($\theta_c = 0°$ and 180°), but fat near the top and the bottom of the cylinder ($\theta_c = \pm 90°$). A single birefringent cord appears at the trailing edge ($\theta_c = 180°$) of the first cylinder and extends along the centerline to the downstream, attributing to the sheared flow between the neighboring cylinders. However, this birefringent cord separates into two branches before the second cylinder, leaving a triangular region of low birefringence in the front of the 'next' cylinder. For the CPyCl:NaSal:NaCl solution, the peak shear rate also occurs at the top and the bottom of the cylinder ($\theta_c = \pm 90°$), but maximal extensional rate is found at the four diagonal corners of the cylinder: $\theta_c = \pm 45°$ and $\pm\,130°$. Although similar distribution of birefringence was highlighted by a crossed polarizer technique,[1] our μPIV result does not reveal the existence of the negative wake as was found in a rising bubble.[35]

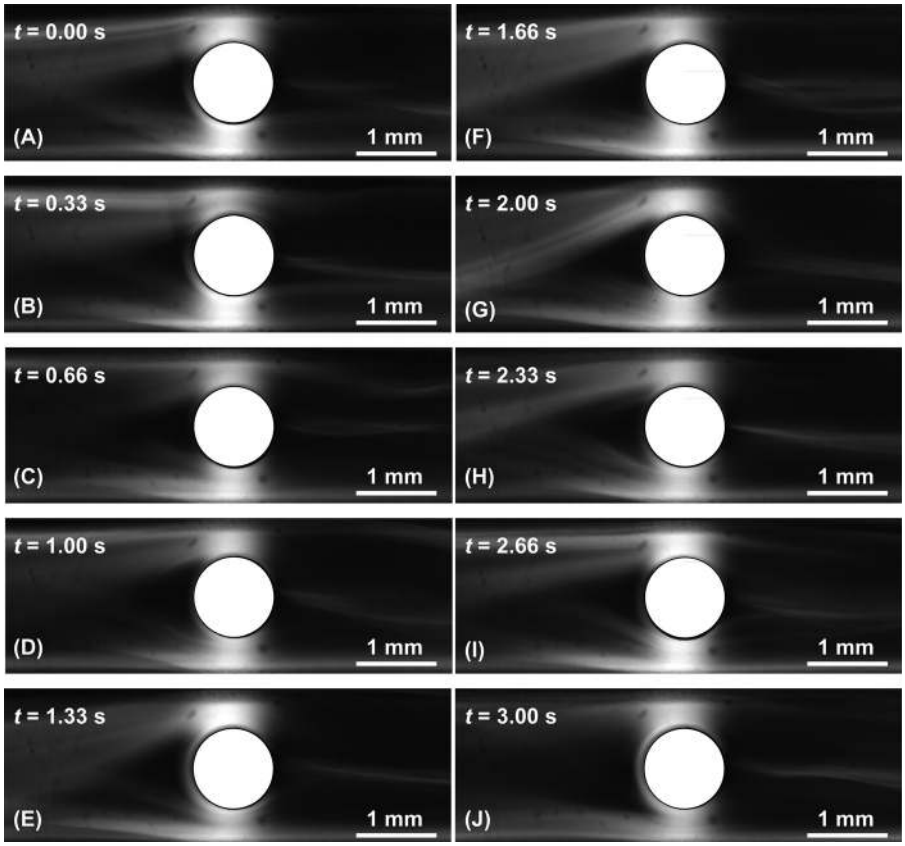

FIG. 7. The sequence of birefringence images for the transient flow of the CTAB:NaSal solution in channel #2, $\varepsilon_0 = 7.4\,s^{-1}$. (Video at 0.33× playback speed). (Multimedia view) [URL: http://dx.doi.org/10.1063/1.4939949.1]

C. Birefringence of transient flow

To demonstrate the capability of the transient measurements of our approach, the sequence of birefringence images for the CTAB:NaSal solution flowing in channel #2 at $\varepsilon_0 = 7.4\,s^{-1}$ is given in Fig. 7 (Multimedia view). As shown in Eq. (9), the light intensity from a single frame can be easily converted to the retardance once the reference image is taken prior to the experiment. Hence, images in Fig. 7 also roughly represent the transient evolution of retardance, which is highly associated with the principal strain rate of the fluid. At this high flow rate, the flow becomes unstable due to the onset of elastic instability. Near the top and the bottom of the cylinder ($\theta_c = \pm 90°$), the shear rate is so large that molecular alignment with the flow is saturated and high retardance region completely occupies the gap all the time. In the upstream region, the emergence of the birefringence strands suggests that high shear exists near the confined wall while the isotropic flow in the middle of the channel is elongational. In the downstream region, we observe a birefringent tail swinging at a frequency of 0.6 Hz. Although the disorderly pattern in the upstream region also blinks with time, its unsteadiness does not display apparent periodicity.

IV. CONCLUSION

In this study, we construct the circular polariscope on top of an inverted microscope by installing two linear polarizers and two quarter waveplates along the light path and use our system to successfully measure the flow-induced birefringence in a microfluidic device. Because of the simple relationship between the light intensity and the retardance, the images acquired by our system provide an intuitive way to visualize the retardance distribution, with which the principal strain in the microflow field can be correlated. In addition, transient measurements can be easily obtained by recording successive images once the reference image is taken prior to the experiment.

For all working fluids tested, there exists a linear region in which the retardance grows linearly with the nominal strain rate. This linearity defines the bounds of a valid range in which the principal strain rate can be correlated to the flow-induced birefringence. For our system, the highest sensitivity can be achieved by using the CPyCl:NaSal solution. Although the CPyCl:NaSal:NaCl solution is less birefringent comparing to the other two fluids, it has the widest measuring range of strain rate. For comparison, we also conduct the μPIV diagnosis to obtain the velocity field, from which the deformation rates of fluid are determined. Pathlines in the microfluidic device are obtained by superpositioning a set of 100 successive μPIV images. We find that regions with large retardance are usually associated with high extensional or shear strain rates so that the distributions of the retardance and the principal strain rate are highly similar. Therefore, we verify that both extensional and shear strain rates contribute to the resultant retardance. In fact, measurement of flow-induced birefringence is able to reveal some flow features that are not detected by conventional methods such as μPIV. While μPIV may lead to large errors in regions with large velocity gradient, high deformation rate can still be resolved by the birefringence approach. In conclusion, our optofluidic approach proves that measurements of flow-induced birefringence provide a non-invasive, transient, full-field quantitation of fluid deformation in a microfluidic environment, from which probing the stress field can be implemented. The proposed method opens a new possibility to diagnose micro-fluid flow from a different aspect, which may offer invaluable insights to the understanding of flow kinematics and helps in better design of microfluidics in the future.

ACKNOWLEDGMENTS

This work was supported by the Ministry of Science and Technology of Taiwan under Grant Nos. NSC 101-2221-E-002-084-MY2 and MOST 102-2221-E-002-245-MY3.

[1]G. R. Moss and J. P. Rothstein, J. Non-Newton Fluid **165**(21–22), 1505–1515 (2010).
[2]R. F. Tuma, W. N. Durán, and K. Ley, *Microcirculation*, 2nd ed. (Academic Press, Boston, MA, 2011).
[3]C. Poelma, P. Vennemann, R. Lindken, and J. Westerweel, Exp. Fluids **45**(4), 703–713 (2008).
[4]C. Poelma, A. Kloosterman, B. P. Hierck, and J. Westerweel, PLOS One **7**(9), e45247 (2012).

[5]C.-Y. Huang, Y. Matsuda, J. W. Gregory, H. Nagai, and K. Asai, Microfluid. Nanofluid. **18**(5), 739–753 (2015).
[6]J. Martel and and B. A. Bruno, in *ASME 2008 International Mechanical Engineering Congress and Exposition* (Boston, MA, U.S.A., 2008), Vol. 10.
[7]T. Schneider, L. Goubergrits, U. Kertzscher, and C. O. Paschereit, in *14th International Symposium on Applications of Laser Techniques to Fluid Mechanics* (Lisbon, Portugal, 2008).
[8]T. J. Ober, J. Soulages, and G. H. McKinley, J. Rheol. **55**(5), 1127–1159 (2011).
[9]S. J. Haward, V. Sharma, and J. A. Odell, Soft Matter **7**(21), 9908–9921 (2011).
[10]S. J. Haward and G. H. McKinley, Phys. Rev. E **85**(3), 031502 (2012).
[11]T. J. Ober, S. J. Haward, C. J. Pipe, J. Soulages, and G. H. McKinley, Rheol. Acta **52**(6), 529–546 (2013).
[12]J. W. Dally and W. F. Riley, *Experimental Stress Analysis* (McGraw-Hill, New York, 1965).
[13]J. Pathak and S. D. Hudson, Macromolecules **39**(25), 8782–8792 (2006).
[14]C. L. Riddiford and H. G. Jerrard, J. Phys. D: Appl. Phys. **3**(9), 1314–1321 (1970).
[15]S. P. Carrington, J. P. Tatham, and J. A. Odell, Polymer **38**(16), 4151–4164 (1997).
[16]J. A. Odell and S. P. Carrington, J. Non-Newton Fluid **137**(1–3), 110–120 (2006).
[17]G. R. Moss and J. P. Rothstein, J. Non-Newton Fluid **165**(1–2), 1–13 (2010).
[18]M. Chilcott and J. Rallison, J. Non-Newton Fluid **29**, 381–432 (1988).
[19]A. W. Liu, D. E. Bornside, R. C. Armstrong, and R. A. Brown, J. Non-Newton Fluid **77**(3), 153–190 (1998).
[20]S. Kenney, K. Poper, G. Chapagain, and G. F. Christopher, Rheol. Acta **52**(5), 485–497 (2013).
[21]H. Janeschitz-Kriegl, *Polymer Melt Rheology and Flow Birefringence* (Springer-Verlag, Berlin, 1983).
[22]G. G. Fuller, *Optical Rheometry of Complex Fluids* (Oxford University Press, New York, 1995).
[23]S. Guo, J. Zhang, L. Wang, J. S. Nelson, and Z. Chen, Opt. Lett. **29**(17), 2025–2027 (2004).
[24]B. K. Wilson and L. Y. Lin, J. Microelectromech. Syst. **17**(4), 1039–1046 (2008).
[25]Z. Wang, A. A. Volinsky, and N. D. Gallant, J. Appl. Polymer Sci. **131**(22), 41050 (2014).
[26]D. B. Murphy and M. W. Davidson, *Fundamentals of Light Microscopy and Electronic Imaging*, 2nd ed. (Wiley-Blackwell, Hoboken, New Jersey, 2013).
[27]D. L. Hu, T. J. Goreau, and J. W. M. Bush, Exp. Fluids **46**(3), 477–484 (2009).
[28]J. Kim, L. Martinelli, K. Lahlil, J.-P. Boilot, T. Gacoin, and J. Peretti, Appl. Phys. Lett. **105**, 061102 (2014).
[29]M. Raffel, C. E. Willert, S. T. Wereley, and J. Kompenhans, *Particle Image Velocimetry: A Practical Guide*, 2nd ed. (Springer, Heidelberg, Germany, 2007).
[30]G. H. McKinley, in *Transport Processes in Bubbles, Drops, and Particles*, edited by D. De Kee and R. P. Chhabra (Taylor & Francis, New York, 2002).
[31]W. Thielicke and E. J. Stamhuis, J. Open Res. Software **2**(1), e30 (2010).
[32]J. R. Taylor, *An Introduction to Error Analysis*, 2nd ed. (University Science Books, Sausalito, CA, 1997).
[33]C. Masselon, J.-B. Salmon, and A. Colin, Phys. Rev. Lett. **100**(3), 038301 (2008).
[34]H. T. Huang, H. E. Fiedler, and J. J. Wang, Exp. Fluids **15**(3), 168–174 (1993).
[35]D. Funfschilling and H. Z. Li, Chem. Eng. Sci. **56**(3), 1137–1141 (2001).